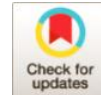




# Nano-Structural Characteristics and Optical and Electrical Properties of Obliquely Deposited Manganese Oxide Thin Films

Fatemeh Chahshouri<sup>1\*</sup>, Elehe Khani<sup>2</sup>, Hadi Savaloni<sup>3</sup> and Rojan Savari<sup>4</sup>



<sup>1,2,3</sup> School of Physics, College of Science, University of Tehran, North-Kargar Street, Tehran, Iran.

**\*Corresponding Author:**

chahshourif@gmail.com

**Received:** 15 September, 2021

**Accepted:** 30 October, 2021

**Published:** 25 December, 2021

## ABSTRACT

In this work, manganese oxide thin films as a graded helical square tower-like (terraced) sculptured thin films with 8, 9, and 10 arms were deposited on a glass substrate by oblique angle deposition (OAD) method. Structural and morphological characteristics of the produced samples were obtained through x-ray diffraction (XRD), atomic force microscopy (AFM), and field emission electron microscopy (FESEM) analyses. The optical and electrical properties of manganese oxide thin film were studied by Photoluminescence (PL), UV-visible (UV-VIS), and V-I measurement. The spectrophotometry analysis on both s-and p-polarized lights at 90° incident light angles carried out for obtaining the optical spectra of the samples. Then, it used to calculate refractive index, energy gaps, and absorption peaks. Photoluminescence spectra for MnO films showed a 2.31, 2.28, and 2.26 eV gap energy in 8, 9, and 10 arms. The electrical resistance measurements of these samples showed that the resistance has strongly dependent on the intensity and energy of the incident light. The electrical resistance of these samples was also investigated under green, blue, red, and light radiation with 100 watts/cm<sup>2</sup> power density.

**Keywords:** MnO, Oblique angle deposition, Nano sculptured layer, Annealing, Optical and electrical behavior

## Introduction

Manganese is a transition metal which has multiple potential oxidation states such as MnO, MnO<sub>2</sub>, and Mn<sub>2</sub>O<sub>3</sub>. Manganese oxide (MnO) is one of the oxide states attracted many applications in industry due to the facility synthesis, inexpensive, nontoxic and semiconductor properties [1-3]. Manganese oxide used in electrode material [4], current signal sensing and thermal insulation [5], rechargeable micro-batteries [1, 6], supercapacitors [2, 3], electrochemical capacitors and sensors [7], magneto-electronic devices [3], gas and screen-printed sensor [6, 8, 9], and catalysts in chemical reactions [9]. In nowadays, manganese oxide thin films absorb much attention in optoelectronic applications because of their bandgap in visible region [1, 3, 10- 13].

The particle size and anisotropy are essential parameters in determining the properties of the nanostructure. For example, it has been reported that MnO nanoclusters show ferromagnetic character, while antiferromagnetic nature is possessed by bulk MnO [14]. Hence, fabrication technique and growth conditions are essential in the production of nanostructures. Diverse physical and chemical deposition techniques have been used for synthesis manganese oxide such as spray pyrolysis [13], sol-gel [15], atomic layer deposition [12], thermal evaporation [5, 9, 12], pulsed laser deposition [1, 2, 16], RF magnetron sputtering [17, 18], metal- organic chemical vapor deposition [19], and electron beam technique followed by annealing post-treatment [20]. Nelson et al. have created manganese oxide thin films by ALD (Atomic layer deposition), and they studied the effects of the deposition temperature and substrate [10].

Also, Thirumalairajan et all, have fabricated MnO thin films by chemical spray pyrolysis at different substrate temperature. they showed MnO are well suited for optoelectronic applications, such as solar energy conversion due to its optical and electrical properties, as well as its chemical and mechanical stability. The optical band gap in this work was 2.33 eV [13].

In Hendi work, Thin films of manganese oxide were deposited by thermal reactive evaporation of pure manganese at room temperature under various oxygen partial pressures. After that, based on the structural and chemical characterizations of them, the optical properties (refractive index and extinction coefficient) of the stoichiometric MnO<sub>2</sub> film was investigated [10]. In the following studies, we grow MnO thin film by electron gun deposition technique. Since PVD synthesis has the number of advantages such as easy preparation, flexibility to obtained required size, and desired shape for nano-structure, we grow MnO nano-structure by e-beam PVD method.

In current years, there are two techniques for controlling the size and shape of nanostructures. oblique angle deposition (OAD) (vapor incident angle less than 85°) and glancing angle deposition (GLAD) (vapor incident angle greater than 85°) of thin films. As a physical vapor deposition method have provided facilities for production of variety of anisotropic nanostructures, which can be controlled by growth parameters such as vapor incident angle, rate of vapor and substrate rotation [21-23].

Sculptured thin films consist of columnar structures which their growth is being controlled by movement of the substrate. Complex structures such as nano-star [24, 25], chiral nano-zigzag [26], nano-square [27], chiral nano-flower [28] shaped sculptured thin films are produced, and their optical properties are investigated both experimentally [28], and theoretically [29-31].

3D sculptured nanostructures fabricated by these methods have a vast area of applications such as optical filters [32], reflectors [33], polarizers [34], sensors [35, 36], bio-scaffolds [37], and micro-channels [38].

In this work, MnO sculptured thin films was fabricated in two steps. First, oblique angle deposition technique, together with the rotation of the substrate sequentially by 90°, while a shadowing block was fixed at the center of the substrate holder, for producing Mn nano-square-structures on glass substrates. Then, Mn thin films were annealed under oxygen gas flow. Morphological, structural, electrical, and optical properties of the samples were investigated.

## Experimental Details

The graded helical square tower-like (terraced) sculptured (GHSTTS) Mn thin films were deposited on glass (microscope slide) substrates. The purity of Mn was 99.99%. An Edwards (Edwards E19 A3) coating

plant with a base pressure of  $8 \times 10^{-7}$  mbar was used prior to deposition; the substrates were ultrasonically cleaned in heated acetone, then ethanol. The deposition angle was fixed at 85°, and the substrate was rotated clock-wise for 90° azimuthally for production of each arm of the GHSTTS. The substrate holder system is controlled by two stepping motors, which can rotate the substrate holder by the two angles,  $\alpha$ , and  $\varphi$ , with 0.01° step accuracy and with controlled speed. The movement of the stepper motor for rotation of substrate about its surface normal ( $\varphi$ ) and its rate of revolution as well as the facility for dividing each revolution to different sectors was controlled through interface to a computer in LABVIEW software. The substrate holder was a stainless-steel disc of 12 cm diameter. At the center of this disc (a cylindrical block 2 cm in diameter and 2 cm in height) was fixed as a shadowing block. The substrates were fixed at 5 cm distance from this shadowing block.

Knowledge from previous work [39] showed, this layer have small grain size, few void fractions, and significant height that it is proper in resistivity and sensitivity properties of thin films.

GHSTTS Mn thin films consisting of eight, nine, and ten arms were produced (Figure 1, and 2). Each arm of the first pitch was deposited for 110 nm, when each arm of the second was 72 and third pitches 36 nm, respectively. The deposition rate was fixed at  $1.0 \text{ \AA}^\circ \text{ s}^{-1}$ . The deposition rate was measured by a quartz crystal deposition rate controller (Sigma Instruments, SQM-160, USA) positioned close to the substrate holder and at the same azimuthal angle as that of the substrate. The surface roughness of the substrates was measured by a Talysurf profilometer, and an AFM and the rms (root mean square) substrate roughness (Rq) obtained using these methods were 0.3 and 0.9 nm, respectively. Oxidation Process for Mn GHSTTS was done at a cylindrical horizontal quartz tube furnace (Exciton, 1200-30/6, T.H, Iran equipped with Shinko temperature programmable controller – PCD 33A) by oxygen gas flow with 99.999% purity. The flow rate of oxygen gas for annealing was in 250 sccm and at 220 °C. A three-stage annealing process was used as; (1) 1.5 hour to reach the set annealing temperature 220 °C (2) samples were kept at the pre-set annealing temperature for 4 hours, (3) they were cooled down to room temperature. The cooling procedure of the samples took place inside the quartz tube of the furnace with the same flow rate of the annealing gas during the annealing process, which took about 2h.

The deposition process was repeated a few times, and the reproducibility of the results was confirmed.

In order to obtain the crystallographic structure of the samples a STOE model STADI MP Diffractometer, Germany (CuK $\alpha$  radiation) with a step size of 0.01° and count time of 1.0 s per step was employed, while the surface physical morphology and roughness was

obtained by means of Atomic force microscope (AFM; Scanning probe, model BL 022 NT-MDT) with a Si tip of 10 nm diameter and in non-contact mode.

The electrical measurements of these thin films were obtained by two-point probe I-V measurement made by the company of Nano pajouhan raga, Iran.

The optical spectra of the samples were obtained using an Ultraviolet-Visible Spectrometer (Varian cary-

500) in the spectral range of (350-850) nm using both s and p polarization measurements.

PL spectra were measured by a Perkin Elmer model of LS 45 fluorescence the spectrophotometer photoluminescence was excited at 400 nm by a single monochromatic line (spectral half width of 5 nm) selected from the continuum emission spectrum of Xe lamp. PL measurements were carried out in the wavelength range of 400-1100 nm at room temperature.

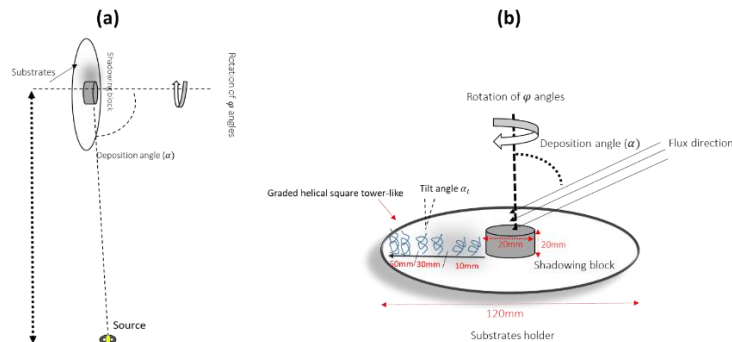


**Figure 1.** a) a shadowing block fixed at the center of the substrate holder; b) Production of graded helical square tower-like (terraced) sculptured thin films.

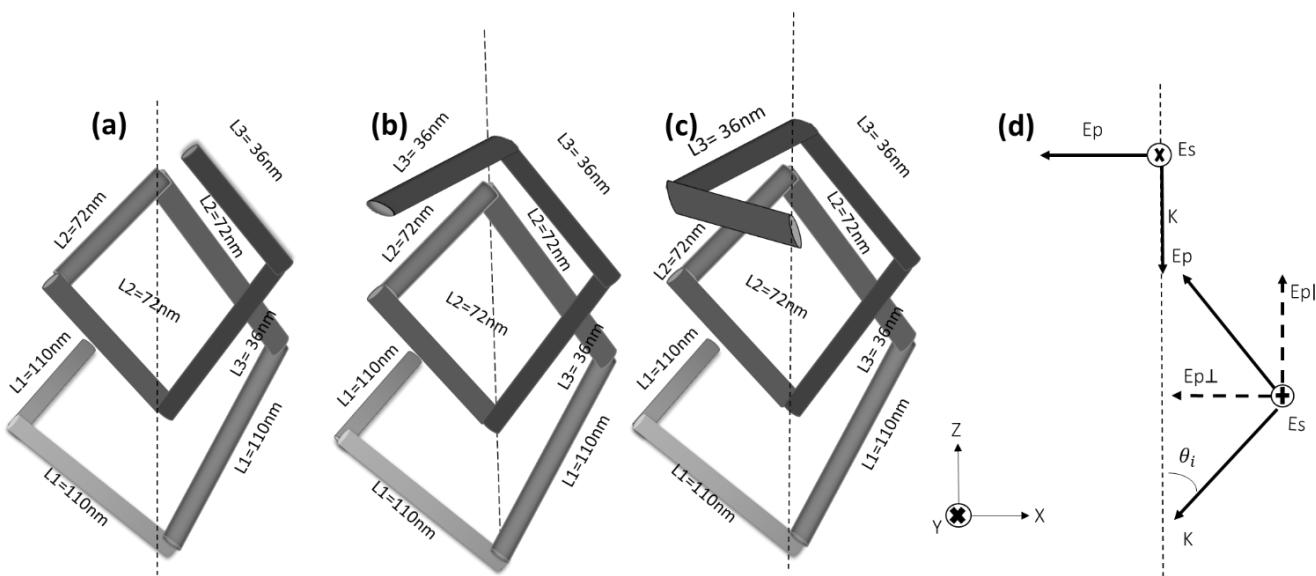


**Figure 2.** Simulation figures of the helical square structure with the corresponding view directions for a) 8, b) 9, and c) 10 arms. L is the length of each nano-rod, respectively. d) The definition of the incident polarization directions as well as decomposition of the p-polarized field by changing the light incident directions shown in.

## Results and Discussion

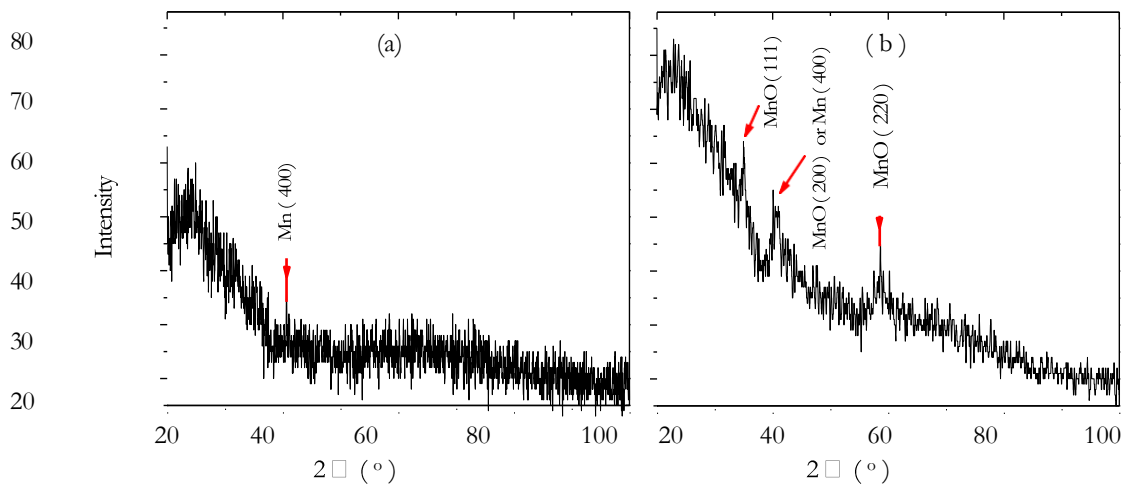
### Crystal structure analysis

Fig. 3 shows the XRD patterns of Mn GHSTTS and MnO GHSTTS on the glass substrate. Mn GHSTTS XRD pattern in Fig. 3 (a) shows the only peak at 40.62° that refers to Mn (400) according to JCPDS cards for

Mn 00-003-0991. Low intensity of this single peak indicates that polycrystalline Mn thin film deposited on glass substrate. Fig. 3(b) shows the XRD patterns of MnO GHSTTS on the glass. The XRD show peaks at 34.95°, 40.62°, and 58.65° that are accordance with the JCPDS cards for to MnO (No: 01-078-0424, 01-075-1090 and 01-077-2363). This results can be assigned to MnO(111), MnO(200), and MnO(220), respectively.

The peaks at  $40.62^\circ$  may also be referred to Mn (400) according to JCPDS cards for Mn 00-003-0991. Peaks intensities in Fig. 3(b) indicate that MnO GHSTTS thin

films have a polycrystalline structure with maximum intensity for the MnO(200) orientation, which has the lowest surface energy in fcc structures.



**Figure 3.** X-ray diffraction patterns of MnO Nano sculptured thin films with different number Arms on a glass substrate a) Mn layer, b) MnO layer.

#### Morphological analysis

Fig. 4 shows the 3D, 2D AFM images and surface void fractions of MnO sculptured thin film. The mean surface roughness, the average grain size of the graded helical square tower-like, and percentage of the surface void fraction of this film were obtained from the

analysis of the AFM images using WSXM and Microvision software.

FESEM images of the surface of graded helical square tower-like (terraced) MnO sculptured thin films are shown in Fig. 5 respectively, the growth angle and the height of all samples are measured by Image J. All information brings together in Table 1.

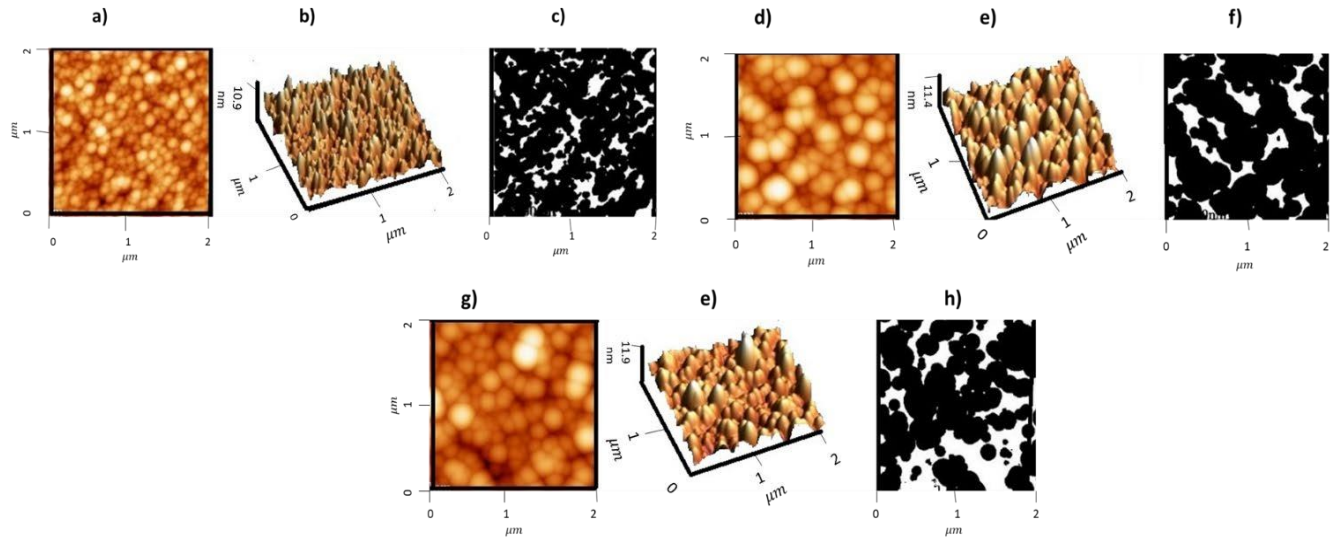


**Figure 4.** 2 and 3D AFM images of graded helical square tower-like (terraced) sculptured manganese oxide thin films a, b, c) 8 Arms, d, e, f) 9 Arms, g, e, h) 10 Arms.

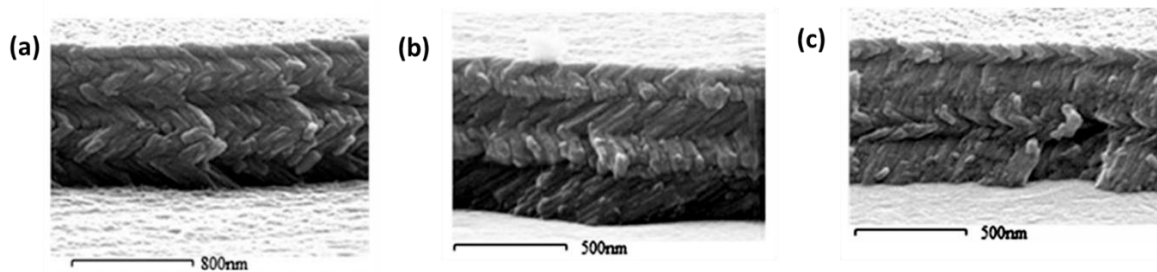


**Figure 5.** FESEM images of graded helical square tower-like (terraced) MnO sculptured thin films produced at 5cm distances from the edge of the shadowing block.

**Table 1**

Details of structural parameters for three Nano sculpture.

Sample	Distance from the shadowing block (cm)	Film thickness (nm)	Helical column tilt angle (at) (°)	DAFM (nm)	Rave (nm)	VFsurf (%)
8 Arms	5	554.6	4	102.0	1.50	8
9 Arms	5	545.4	4	96.0	2.03	11.56
10 Arms	5	531.0	3	91.9	1.65	17.55

#### Optical results

The reflection, transmission, and absorption spectra measured for both s- and p-polarized lights in MnO thin films are given in Fig. 6(a) and 6 (b), respectively.  $T_s$  and  $T_p$  are related to the transmission spectra in both s- and p-polarized lights, respectively the corresponding reflection spectra are assigned by  $R_s$  and

$R_p$  while  $A_s$  and  $A_p$  indicate the absorption spectra for two polarized lights. Such a sharp absorption occurs due to electron excitation from filled to the empty band. The relation between reflected, transmitted and absorbed light is considered as:

$$TT+RR+AA=1, \quad (1)$$

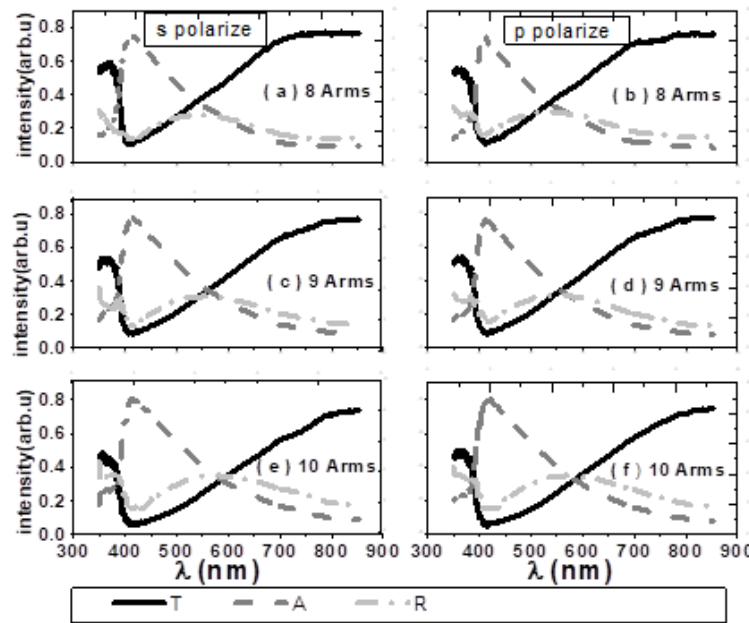


**Figure 6.** Optical Spectra (reflection, transmission, and absorption) s and p-polarizations of graded nano sculptured

From previous work can be seen that the reflection and transmission for the Mn [39] Thin film are negligible (~5%, 6%, 3% and 4% for  $T_s$ ,  $T_p$ ,  $R_s$ , and  $R_p$ ,

respectively), while it shows high absorption (~91% and 89% for  $A_s$  and  $A_p$ , respectively). After light

illuminating on the surface of the metal, metal-free collectively, which is known as the surface Plasmon oscillation [40]. Comparison of optical spectra of the un-annealed sample (Mn) [39] with the annealed sample by oxygen (MnO) shows the fact that the annealing process increased the intensity of transmission and reflection. In accordance to the reflection and transmission spectra, there isn't any difference between R and T for both P and S polarization. In manganese oxide layers, the identical behavior in both polarizations implies homogeneous and isotropic properties of MnO sculptured layers. After the annealing process because of interaction between oxygen and surface, the porosity was decreased (Oxigens filled the surface hole). This phenomenon caused the transitions of the samples from metal to oxide semiconductor according to XRD results.

Furthermore, the extinction coefficient  $k$ , which

represents the value of the absorbed light in the thin film, can be calculated by equation (2).

$$\exp(-4\pi n k \lambda / d) = (2)$$

Where  $\lambda$  is the wavelength of the incident light, and  $d$  is the thickness of the thin film [21]. The real refractive index ( $n$ ) was calculated by equation (3) [41].

$$(1+R) + \frac{4k}{4k - k^2}, (3)$$

Fig. 7 shows  $n$  and  $k$  spectrums. In the previous paper [39], it has been showed that the behavior of the extinction of squared nano-structure is unusual in experimental measurements. While, in MnO the variation of wavelength caused changes in the refractive index. These changes proved these layers are dispersive.

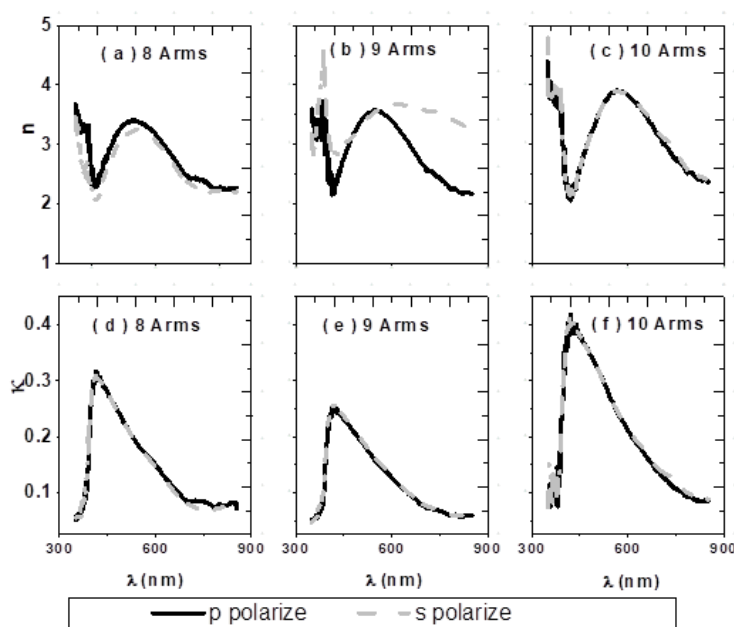


**Figure 7.** Real and imaginary parts of the refractive index of graded helical MnO sculptured thin films with different number of Arms on glass substrates.

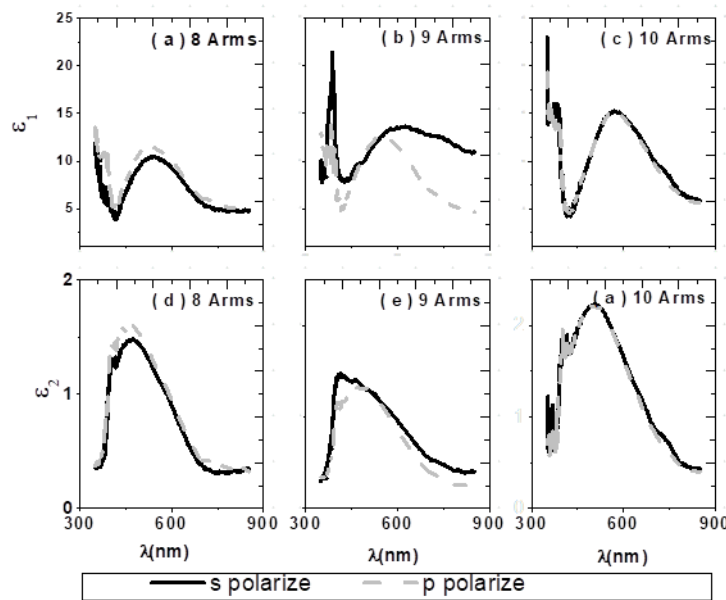
Fig. 8 shows the real ( $\epsilon_1$ ) and imaginary ( $\epsilon_2$ ) parts of the dielectric constant spectrums. These constants were also calculated by equation (4) and (5) [42].

$$\epsilon_1 = n^2 - k^2, (4)$$

$$\epsilon_2 = 2nkn, (5)$$

Where  $\epsilon_1$  is the real part of the dielectric constant and indicates the stored energy of the dielectric constant, and  $\epsilon_2$  is the imaginary part of the dielectric constant, and it is corresponding to the energy loss in the environment [43]. As seen in Fig. 8, the real part of the

dielectric constant is higher than of the imaginary part. In low frequency, the real refractive index is too bigger than the extinction coefficient. Therefore, the lattice portion overcomes to dielectric polarization; for this reason, the behavior of the layer is the same as a simple dielectric  $\epsilon\epsilon_1 \approx nn2$ . One weak absorption in accordance with  $\epsilon\epsilon_2$  shows radiation absorption by means of free career, whereas, In  $\lambda\lambda < 500nnnn$  the fluctuation in  $n$  and  $k$  shows the lattice portion is conquer.



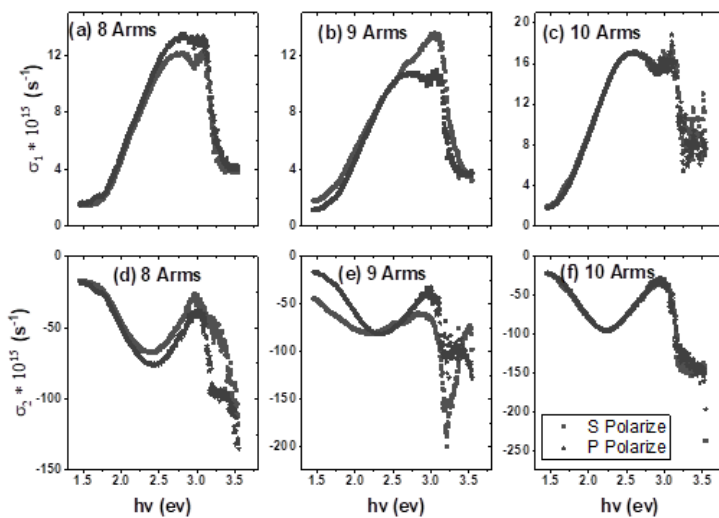
**Figure 8.** Plots of the real and imaginary part of the dielectric constants versus wavelength obtained for the MnO films for different arms.

Fig. 9 shows the result of calculations of the conductivity  $\sigma_1 + i\sigma_2$  obtained from values of  $\epsilon_1$  and  $\epsilon_2$  which is obtained by equation (6) and (7) [42]. The conductivity is usually plotted because it remains finite wherever  $\epsilon_2$  is infinite. This procedure makes the

structures in the optical constants at low frequencies more pronounced. The real  $\sigma_1$  and imaginary  $\sigma_2$  parts of conductivity are given as:

$$\sigma_1 = \epsilon_2 \omega 4\pi \quad (6)$$

$$\sigma_2 = (1 - \epsilon_1) \omega 4\pi \quad (7)$$



**Figure 9.** a, b, and c) real part of conductivity constants and, d, e, f) imaginary part of conductivity constants versus energy (eV) for Mn/glass thin films deposited at different arms with flow of oxygen.

The conductivity spectra in Fig. 9(a, b, and c) show a peak with the onset of about 3.0 eV for the annealed

sample with 9 Arms, which is shifted to lower and higher energies at other arms of 8 and 10, respectively.

The intensity of this peak is also increased in the same Bandgap (Eg) is an important parameter to determine the application and electronic properties of thin films. Semiconductors have a direct or indirect bandgap. In direct bandgap, conduction and valance band are in the same momentum. Hence, electron just absorb a photon for exciting, but at the indirect bandgap, electron needs to absorb phonon in addition to the photon. The bandgap of the MnO graded helical square tower-like (terraced) sculptured (GHSTS) thin film was calculated by two approaches: (i) Tauc method and (ii) [44, 45], and photoluminescence spectrum. In first approach, equation (8) was used for calculating absorption coefficient ( $\alpha$ ), and equations (9) give relationship between  $\alpha$  is and Eg.

$$\pi\pi = \square, \quad \square \quad (8)$$

**Table 2**  
Calculated Band gap energy for samples in a different procedure.

Sample	Eg (PL)	Eg (direct)	Eg (indirect)
8 Arms	2.31	2.53	1.29
9 Arms	2.28	2.43	1.42
10 Arms	2.26	2.34	1.31

Thickness of the films was the reason for decreeing bandgap energy by increasing the number of arms, which is attributed to the improvement in the crystal structures, morphological changes, and crystallite size. There is a possibility of structural defects in the thin films due to their growth at different arms (8, 9, and 10); this could give rise to the allowed states near the conduction band in the forbidden region. In the case of

order of 10 arms nano sculpture.

$$(\alpha h\nu)^r = B(h\nu - E_{gg}), \quad (9)$$

Where B is a constant, h is plank constant,  $\square$  is frequency of incident light and the constant r is an index that characterizes transitions of electron for absorption process (i.e.,  $r = 1/2$  (indirect transition),  $r = 2$  (direct transition),  $r = 2/3$  (unpermitted direct transition) and  $r = 2/3$  (unpermitted indirect transition) [32]). By extrapolating  $(\alpha h\nu)^r$  plot versus  $h\nu$  in Fig. 8(a, b, c), the band gap values were calculated for direct (Fig. 10 (a, B, c, e)) and indirect (Fig. 10(b, d, f)) band gap for both s and p polarization. Results of calculating Eg by two approaches were shown in Table2.

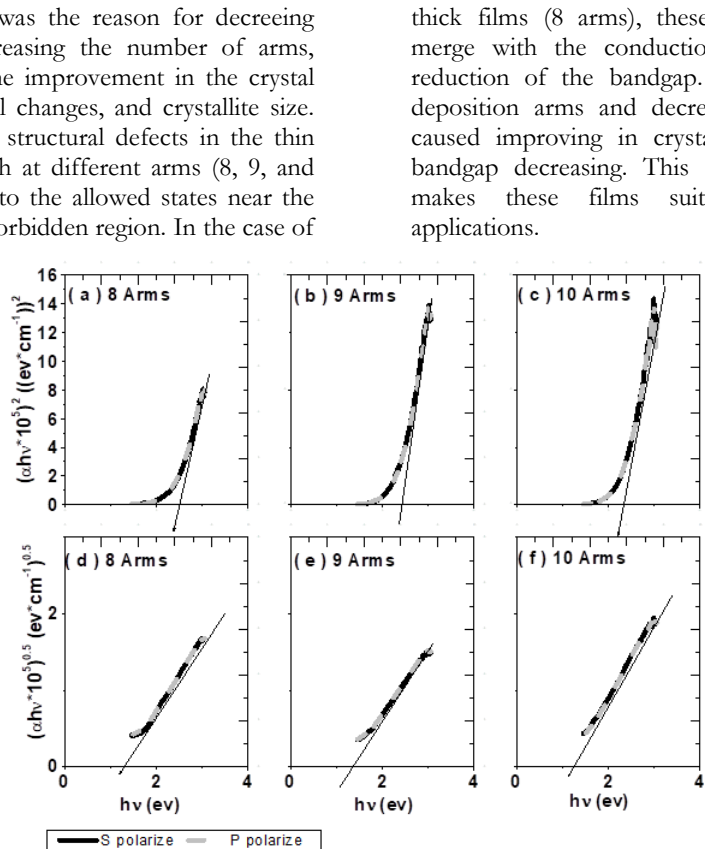


**Figure 10.** Band gap of graded helical MnO sculptured thin films with different number of Arms on glass substrates.

In a typical PL experiment, a semiconductor was excited with a light source which provides photons energy

thick films (8 arms), these allowed states may well merge with the conduction band, resulting in the reduction of the bandgap. Similarly, an increase in deposition arms and decrease in the film thickness caused improving in crystalline structures along the bandgap decreasing. This optical bandgap widening makes these films suitable for optoelectronic applications.

larger than the band-gap energy. Therefore, the electrons obtain enough energy to recombine with spectrum was recorded in the range of (400-1100) nm as shown in Fig. 11. The sample was excited at 400nm. Photoluminescence results of the layer with different arms show a small peak emitted in the blue light spectrum and high-intensity peak in the green spectrum. These results indicate that MnO films have blue and green fluorescence emission.

According to Fig. 11. near the original peak (transition regarding to impurity and electron movement between donor/acceptor band) the weak peak with bigger wavelength was observed. That is related to the exciton luminescence. Exciton state is located lower than the conduction band and in vicinity of donor state. for this reason, the exciton spectrum have a sharp peak in bottom of the absorption peak, the exciton energy in these samples was 2.58-2.71 ev. These results showed adding new arms in nanostructure changes energy difference between conduction and valance band.

holes under the emission of photons. The excitation

These changes have occurred because of the effect of extra arms with 90degree rotation and parameters such as surface roughness and grain size (number of grain boundaries). These results showed the layer with biggest roughness have minimum bandgap.

Also, in this figure a strong peak at  $\lambda\lambda = 800nnnn$  was observed, this peak is related to the glass substrate, the glass is transparent in the visible spectrum, but its absorbance is in the ultraviolet and infrared range spectrum. Our PL results are compatible with Thirumalairajan work [13],  $E_g$  was 2.33 from photoluminescence study. A low difference between them is relative to average crystallite size which was in Thirumalairajan's work 26.509 nm. Reducing the crystallite size gaps, increasing the arms distance. Therefore, bandgap increase.

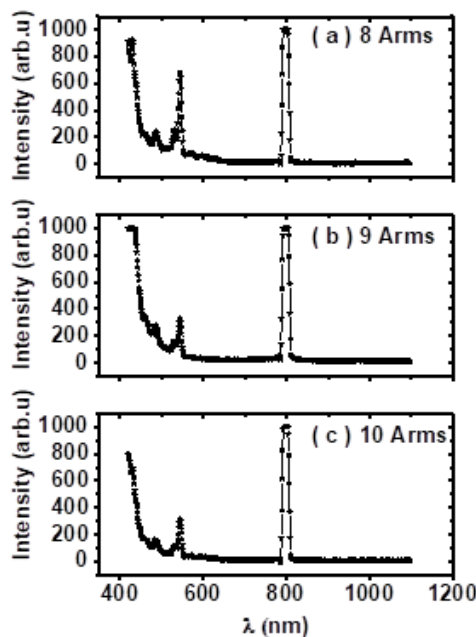


**Figure 11.** Photoluminescence spectrum for graded helical Nanostructure with different Arms a) 8 Arms, b) 9 Arms, c) 10 Arms.

#### Electrical measurements

Photoconductivity is increasing in the conductivity of the semiconductor layer by radiation the light beam onto it. This process done because of electron exciting in forbidden gap. Increasing the number of free careers increase conductivity. The main condition for electron exciting is  $E_g < h\nu$ . When electrical current passed through semiconductor thin films, and light beam irradiated vertically over it, the free electron-hole pair (minority career) produced. Before light radiation, the conductivity is  $\sigma_0 = e(m_0\mu_{ee} + p_0\mu_{hh})$ ,  $m_0$ ,  $p_0$  is electron,

an hole density in equilibrium state. After light radiation, career density increase  $\Delta n$ ,  $\Delta p$ . In this case, In addition to drift effect in resistivity, the effect of minority career was affected on resistivity  $\sigma n_{neenn} = e(\mu_{ee} + \mu_{hh}) + \sigma_0$ ,  $\mu_{ee}$  and  $\mu_{hh}$  are electron-hole mobility.

In this study, the two-point probe instrument with (-5, 5 volts) voltage was used for calculating the resistance of MnO film deposited on glass substrate. The film was pasted with silver to ensure ohmic contacts. Fig. 12 shows the I-V curve for this layers in dark, light bulb with 100 W/cm<sup>2</sup> power, and in the exposing of other

led light. Upon photoillumination, electron-hole pairs are created by absorption of photons, which have energy greater than the bandgap of the MnO, as response in front of the red, green, and blue lights with 100 W/cm<sup>2</sup> power was done. Based on current-voltage curve, resistance under illumination of different light

illustrated in Fig. 12. These charge carriers can reach the MnO surface quickly. After that, in the second step V-I sources was calculated. all results of electrical response for these layers reported in Table 3.

**Table 3**  
Electrical resistance for thin-film Nano sculpture.

Sample	$\rho$ dark (G $\Omega$ .cm)	$\rho$ Light (G $\Omega$ .cm)	$\rho$ Red (G $\Omega$ .cm)	$\rho$ Green (G $\Omega$ .cm)	$\rho$ Blue (G $\Omega$ .cm)
8 Arms	0.080399	0.006772	0.00592	0.00495	0.004472
9 Arms	0.080399	0.006778	0.006182	0.005392	0.004699
10 Arms	0.080399	0.006778	0.005255	0.004865	0.004283

Thin films resistivity is a function of different parameters, such as surface scattering, grain boundary, impurities, and different deposition parameters. Therefore, according to the table 3, the best response to the blue light was observed, which is the effect of the observed absorption peak, as well as the results show, different arms in the vicinity of light bulb and dark medium have identical the resistance, but in the vicinity of the single beam of visible spectrum, this behavior is different. In savaloni's paper [27] the resistivity for Mn graded helical tower-like sculptured

are calculated for each arms, in their work, the resistance was in the order of ( $\Omega$ . m), and the resistance was un-isotropic. Fig. 12 shows, the nano sculpture with 9 Arms has the highest resistance. The reason for observing higher electrical reluctance in this layer is related to the interaction of flow of oxygen with extra arms which oxygen absorbs to the head of arms and increase thickness; Therefore, this upper arm loses the freedom of movement. The layer with 9 arms have biggest grain diameter.

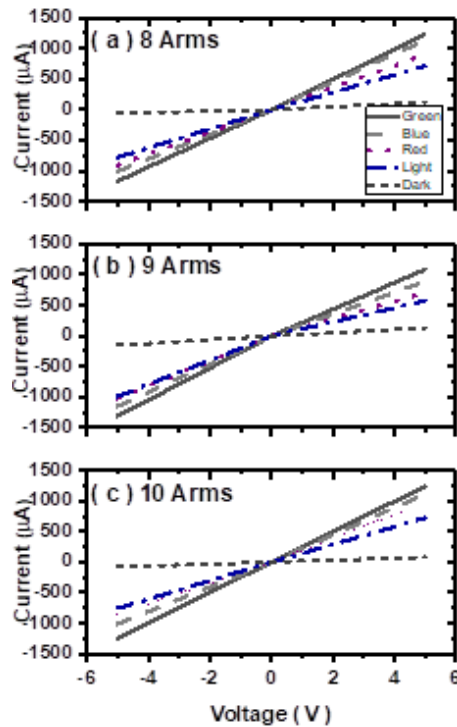


**Figure 12.** Electrical Resistivity of MnO graded helical thin films with different number of Arms (a) 8 Arms, (b) 9 Arms (c) 10 Arms.

## Conclusion

Oblique angle deposition methods in conjunction with the rotation of sample holder with different speeds at different pitches of each revolution were employed to produce Mn-based nano-sculptured thin films. Morphology, nanostructure and crystal structure of the suggest that by engineering the morphology of Mn-based (MnO) films in the form sculptured thin films, broadband optical absorption regions can be obtained in the spectrum with potential applications in trapping of light in photocells and multi-plasmonic.

## References

1. Xia H. et al., Manganese oxide thin films prepared by pulsed laser deposition for thin film microbatteries. *Mater Chem Phys.* 2014; 143(2): 720-727.

2. Yang D. Pulsed laser deposition of manganese oxide thin films for supercapacitor applications. *J Power Sour.* 2011; 196(20): 8843-8849.

3. Staiti P, Lufrano F. Study and optimisation of manganese oxide-based electrodes for electrochemical supercapacitors. *J Power Sour.* 2009; 187(1): 284-289.

4. Sanchez L. et al., Low-temperature mixed spinel oxides as lithium insertion compounds. *J Mater Chem.* 1996; 6(1): 37-39.

5. Baca R. Manganese oxide thin-films for current-signal sensing and thermal insulation. *Mater Sci Semiconduct Proc.* 2013; 16(5): 1280-1284.

6. Gurban AM. et al., Manganese oxide based screen-printed sensor for xenoestrogens detection. *Sensors and Actuators B: Chemical*, 2015; 210: 273-280.

7. Simon P, Gogotsi Y. Materials for electrochemical capacitors, in Nanoscience and Technology: *Collect Rev Nat J. World Sci.* 2010; 320-329.

8. Tian X. et al., Trace level detection of hydrogen gas using birnessite-type manganese oxide. *Sensors and Actuators B: Chemical*, 2015; 207: 34-42.

9. Liu C. et al., Ethanol gas sensing properties of hydrothermally grown  $\alpha$ -MnO<sub>2</sub> nanorods. *J Alloy Compound.* 2017; 727: 362-369.

10. Nilsen O, Fjellvåg H, Kjekshus A. Growth of manganese oxide thin films by atomic layer deposition. *Thin Solid Film.* 2003; 444(1-2): 44-51.

11. Tian HY. et al., Influences of annealing temperature on the optical and structural properties of (Ba, Sr) TiO<sub>3</sub> thin films derived from sol-gel technique. *Thin Solid Film.* 2002; 408(1-2): 200-205.

12. Dakhel A. Correlated structural and electrical properties of thin manganese oxide films. *Thin Solid Film.* 2006; 496(2): 353-359.

13. Thirumalairajan S. et al., Structural and optical investigation of manganese oxide thin films by spray pyrolysis technique. *Optoelectron Adv Mater Rapid Comm.* 2008; 2: 779-781.

14. Lee GH. et al., Anomalous magnetic properties of Mn nanoclusters. *J Am Chem Soc.* 2002; 124(41): 12094-12095.

15. Kim KJ, Park YR. Sol-gel growth and structural and optical investigation of manganese- oxide thin films: structural transformation by Zn doping. *J Cryst Growth.* 2004; 270(1-2): 162-167.

16. Jamil H. et al., Structural and optical properties of manganese oxide thin films deposited by pulsed laser deposition at different substrate temperatures. *Laser Phys.* 2017; 27(9): 096101.

17. Vlakhov E. et al., Influence of the substrate on growth and magnetoresistance of La 0.7 Ca 0.3 MnO<sub>2</sub> thin films deposited by magnetron sputtering. *J Appl Phys.* 1998; 83(4): 2152-2157.

18. Hwang KH, Lee SH, Joo SK. Characterization of sputter-deposited LiMn<sub>2</sub>O<sub>4</sub> thin films for rechargeable microbatteries. *J Electrochem Soc.* 1994; 141(12): 3296-3299.

19. Zhang H. et al., Growth of manganese oxide nanoflowers on vertically-aligned carbon nanotube arrays for high-rate electrochemical capacitive energy storage. *Nano Lett.* 2008; 8(9): 2664-2668.

20. Erlandsson O. et al., Electrochromic properties of manganese oxide (MnO<sub>x</sub>) thin films made by electron beam deposition. 1993; 139: 451-457.

21. Hawkeye MM, Brett MJ. Glancing angle deposition: fabrication, properties, and applications of micro-and nanostructured thin films. *J Vacuum Sci Technol A: Vacuum Surf Film.* 2007; 25(5): 1317-1335.

22. Jensen MO, Brett MJ. Periodically structured glancing angle deposition thin films. *IEEE Trans Nanotechnol.* 2005; 4(2): 269-277.

23. Li H. et al., The morphology and texture of Cu nanorod films grown by controlling the directional flux in physical vapor deposition. *Nanotechnol.* 2008; 19(33): 335708.

24. Babaei F, Savaloni H. Optical absorption transitions in Mn star-like helical sculptured thin films. *Plasmonic.* 2018; 13(1): 203-214.

25. Savaloni H, Goli-Haghghi S, Babaei R. Application of Mn-Cu helical star-shaped (pine- tree-like) sculpted thin films with different symmetries using surface-enhanced raman spectroscopy (SERS). *Appl Spectroscopy.* 2019; 0003702819841913.

26. Savaloni H, Esfandiar A. Fabrication, characterization and some applications of graded chiral zigzag shaped nano-sculptured silver thin films. *Appl Surf Sci.* 2011; 257(22): 9425-9434.

27. Fakharpour M, Savaloni H. Fabrication of graded helical square tower-like Mn sculptured thin films and

investigation of their electrical properties: comparison with perturbation theory. *J Theoretical Appl Phys.* 2017; 11(2): 109-117.

28. Savaloni H, Haydari-Nasab F, Malmir M. Nanostructural characteristics and optical properties of silver chiral nano-flower sculptured thin films. *Appl Surf Sci.* 2011; 257(21): 9044-9055.

nanostructures on shape, dimensions and incident light by discrete dipole approximation. *J Theoretical Appl Phys.* 2012; 6(1): 11.

31. Abdi F, Siabi-Gerjan A, Savaloni H. On the discrete dipole approximation investigation of the extinction spectra of Ag/glass nano-flower thin film with threefold symmetry. *J Theoretical Appl Phys.* 2012; 6(1): 4.

32. Lakhtakia A. Sculptured thin films, in Electromagnetic Materials. *World Sci.* 2005; 97-102.

33. Robbie K. Chiral sculptured thin films. *Nat.* 1996; 384(6610): 616-618.

34. Hodgkinson IJ. et al., Chiral mirror and optical resonator designs for circularly polarized light: suppression of cross-polarized reflectances and transmittances. *Optic Comm.* 2002; 210(3-6): 201-211.

35. Steele JJ. et al., Nanostructured gradient index optical filter for high-speed humidity sensing. *Sensors and Actuators B: Chemical*, 2006; 120(1): 213-219.

36. Esfandiar A, Savaloni H, Placido F. On the fabrication and characterization of graded slanted chiral nano-sculptured silver thin films. *Physica E: Low-dimensional Systems and Nanostructures*, 2013; 50: 88-96.

37. Harris KD. et al., Microchannel surface area enhancement using porous thin films. *J Electrochem Soc.* 2000; 147(5): 2002-2006.

38. Lakhtakia A. et al., Six emerging directions in sculptured-thin-film research. *Adv Solid State Phys.* 2008; 295-307.

39. Savaloni H. et al., Nano-structure and optical extinction spectra and electric field enhancement of silver chiral nano-flower shaped nanoparticle; comparison of discrete dipole approximation results with experimental results. *Eur Phys J B.* 2013; 86(6): 257.

30. Abdi F, Siabi-Gerjan A, Savaloni H. Investigation on the dependence of optical spectra of silver chiral properties (plasmonic) of graded helical square tower-like (terraced) Mn sculptured thin films. *Appl Surf Sci.* 2017; 393: 234-255.

40. Pitarke J. et al., Theory of surface plasmons and surface-plasmon polaritons. *Rep Prog Phys.* 2006; 70(1): 1.

41. El-Nahass M, Farag A, Atta A. Influence of heat treatment and gamma-rays irradiation on the structural and optical characterizations of nano-crystalline cobalt phthalocyanine thin films. *Synthet Metal.* 2009; 159(7-8): 589-594.

42. Gode F, Gurus C, Zor M. Influence of the thickness on physical properties of chemical bath deposited hexagonal ZnS thin films. *J Optoelectron Adv Mater.* 2007; 9(7): 2186.

43. Farea A. et al., Structure and electrical properties of Co<sub>0.5</sub>CdxFe<sub>2.5-x</sub>O<sub>4</sub> ferrites. *J Alloy Compound.* 2008; 464(1-2): 361-369.

44. Ojeda CB, Rojas FS. Recent applications in derivative ultraviolet/visible absorption spectrophotometry: 2009-2011: A review. *Microchem J.* 2013; 106: 1-16.

45. Isik M, Gasanly N. Composition-tuned band gap energy and refractive index in GaS<sub>x</sub>Se<sub>1-x</sub> layered mixed crystals. *Mater Chem Phys.* 2017; 190: 74-78.

46. Krane KS. Modern physics. Modern Physics, 2nd Edition, by Kenneth S. Krane. ISBN 0-471-82872-6. Wiley-VCH, August 1995: 608.

## SJIS

**Copyright:** © 2021 The Author(s); This is an open-access article distributed under the terms of the Creative Commons Attribution License (<http://creativecommons.org/licenses/by/4.0/>), which permits unrestricted use, distribution, and reproduction in any medium, provided the original work is properly cited.

**Citation:** Chahshouri F, Khani E, Savaloni H, Savari R. Nano-Structural Characteristics and Optical and Electrical Properties of Obliquely Deposited Manganese Oxide Thin Films. SJFST, 2021; 3(4): 1-12.

<https://doi.org/10.47176/sjfst..3.4.1>